

Article

Synthesis of Rectorite/Fe₃O₄/ZnO Composites and Their Application for the Removal of Methylene Blue Dye

Huanhuan Wang ¹, Peijiang Zhou ^{1,*}, Rui Guo ¹, Yifei Wang ¹, Hongju Zhan ² and Yunfei Yuan ¹

¹ School of Resources and Environmental Science, Hubei Biomass-Resource Chemistry and Environmental Biotechnology Key Laboratory, Eco-Environment Technology R&D and Service Center, Wuhan University, Wuhan 430079, China; doublewhh@163.com (H.W.); gregoryguo@163.com (R.G.); yifeiwangzyh@gmail.com (Y.W.); yuanyunfei0523@126.com (Y.Y.)

² Chemical Engineering and Pharmaceutical Department, Jingchu University of Technology, Jingmen 448000, China; blackcat927@tom.com

* Correspondence: zhoupj@whu.edu.cn; Tel.: +86-027-6876-6930

Received: 10 February 2018; Accepted: 6 March 2018; Published: 9 March 2018

Abstract: A novel series of rectorite-based magnetic zinc oxide (ZnO) photocatalysts (REC/Fe₃O₄/ZnO) was synthesized and characterized in the present work. The fabricated REC/Fe₃O₄/ZnO composite possessed a high specific surface area and high capacity of adsorption and photocatalysis toward methylene blue (MB) dye. The adsorption isotherm of the dye on the composite fitted well to the Langmuir model, with a maximum adsorption of 35.1 mg/g. The high adsorption capacity increased the interactions between the dye and the REC/Fe₃O₄/ZnO, which enabled efficient decomposition of the dye under simulated solar radiation using REC/Fe₃O₄/ZnO as the photocatalyst. The degradation kinetics of MB dye followed the Langmuir–Hinshelwood model. More importantly, the degradation of MB dye and the mass loss of REC/Fe₃O₄/ZnO after three repetitive experiments were quite small. This suggests that the magnetic composite has great potential as an effective, stable, and easily recovered catalyst. Four major intermediates were detected during the degradation of MB dye and the degradation pathway was proposed.

Keywords: adsorption; magnetic ZnO; methylene blue; photodegradation; rectorite

1. Introduction

Synthetic dyes are used in a wide range of industries, including textiles, cosmetics, printing, pharmaceuticals, and food. Of these dyes, approximately 1–2% and 1–10%, are discharged into the environment by manufacturing processes and end-users, respectively [1–5], which poses a serious threat to human health and the environment. Several physical, chemical and biological techniques have been used to treat dyestuff waste, but the high cost, formation of hazardous coproducts, and intensive energy requirements have limited their extensive application [6]. Additionally, traditional wastewater treatment processes are inefficient in handling dye pollutants because of their biological resistance and chemical stability [7–9]. The removal of dyestuff waste from aqueous solutions is technically very challenging.

Photocatalysis could be an effective wastewater treatment technology for dye pollutants because of its potential high activity, low energy consumption, mild treatment conditions, and ease of handling [10–16]. The irradiation of wide bandgap semiconductors by ultraviolet light produces various reactive oxygen species (ROS) including hydroxyl radicals (•OH) and singlet oxygen (¹O₂), which can efficiently oxidize or mineralize organic compounds. Moreover, direct reaction between valence-band holes and organic pollutants could induce oxidation or decomposition of these target

pollutants. The contributions of ROS and holes toward the degradation of pollutants depend on the electronic properties of the target substance and the photocatalyst [17,18]. Photocatalysis can degrade organic dyes into water, carbon dioxide, and other non-toxic inorganic compounds without causing secondary pollution.

Complementary metal-oxide semiconductors have received significant attention because of their efficient application in photocatalysis such as titanium dioxide (TiO_2), cuprous oxide (Cu_2O), and so on [19,20]. Zinc oxide (ZnO) is a well-known photocatalyst with a bandgap of 3.37 eV that permits the absorption of ultraviolet (UV)-visible light. It also has the advantages of high photoactivity, non-toxicity, and low manufactured cost [21–26]. Photocatalysis using ZnO has been used to remove many pollutants from aqueous solutions because ZnO is effective in producing $\bullet\text{OH}$ [27–29]. However, the application of such photocatalysis to wastewater treatment is limited because of the difficulty in separating and recovering ZnO powder from the treated solutions. Using magnetic heterogeneous catalysts could facilitate efficient, rapid, and economical separation of the photocatalyst [30]. Water treatment agents modified with magnetic nanoparticles are particularly interesting; examples of these materials include magnetic iron oxide/clay composite materials such as magnetite (Fe_3O_4) [31–38] and maghemite ($\gamma\text{-Fe}_2\text{O}_3$) [35,39].

One strategy to improve ZnO performance has focused on the development of ZnO composites that enhance the photocatalytic efficiency via improved adsorption [40–45]. Rectorite (REC), a silicate clay mineral, is composed of alternating pairs of nonexpandable dioctahedral mica-like and expandable dioctahedral smectite-like layers [46]. REC efficiently adsorbs organic compounds both on its external surfaces and within its interlaminal spaces because of its high specific surface area and ion exchange properties [47]. This mineral is also of considerable interest as a catalyst support because of its low cost, small size, and unusual intercalated structure. Consequently, considerable research has been devoted to exploring the use of REC-based materials to adsorb or catalytically decompose environmental pollutants [48–51].

In this study, REC/ Fe_3O_4 was prepared by mixing REC with Fe_3O_4 . This was further mixed with ZnO to obtain a REC/ Fe_3O_4 / ZnO composite via an improved hydrothermal process. The composite was characterized by transmission electron microscopy (TEM), scanning electron microscopy (SEM), X-ray powder diffraction (XRD) and Fourier transform-infrared (FT-IR). The absorption and photocatalytic properties of REC/ Fe_3O_4 / ZnO were evaluated by the decomposition of methylene blue (MB) dye under simulated sunlight irradiation. Such a composite material has potential as a new low-cost and recyclable agent for the efficient eliminate treatment of dyestuff wastewater.

2. Results and Discussion

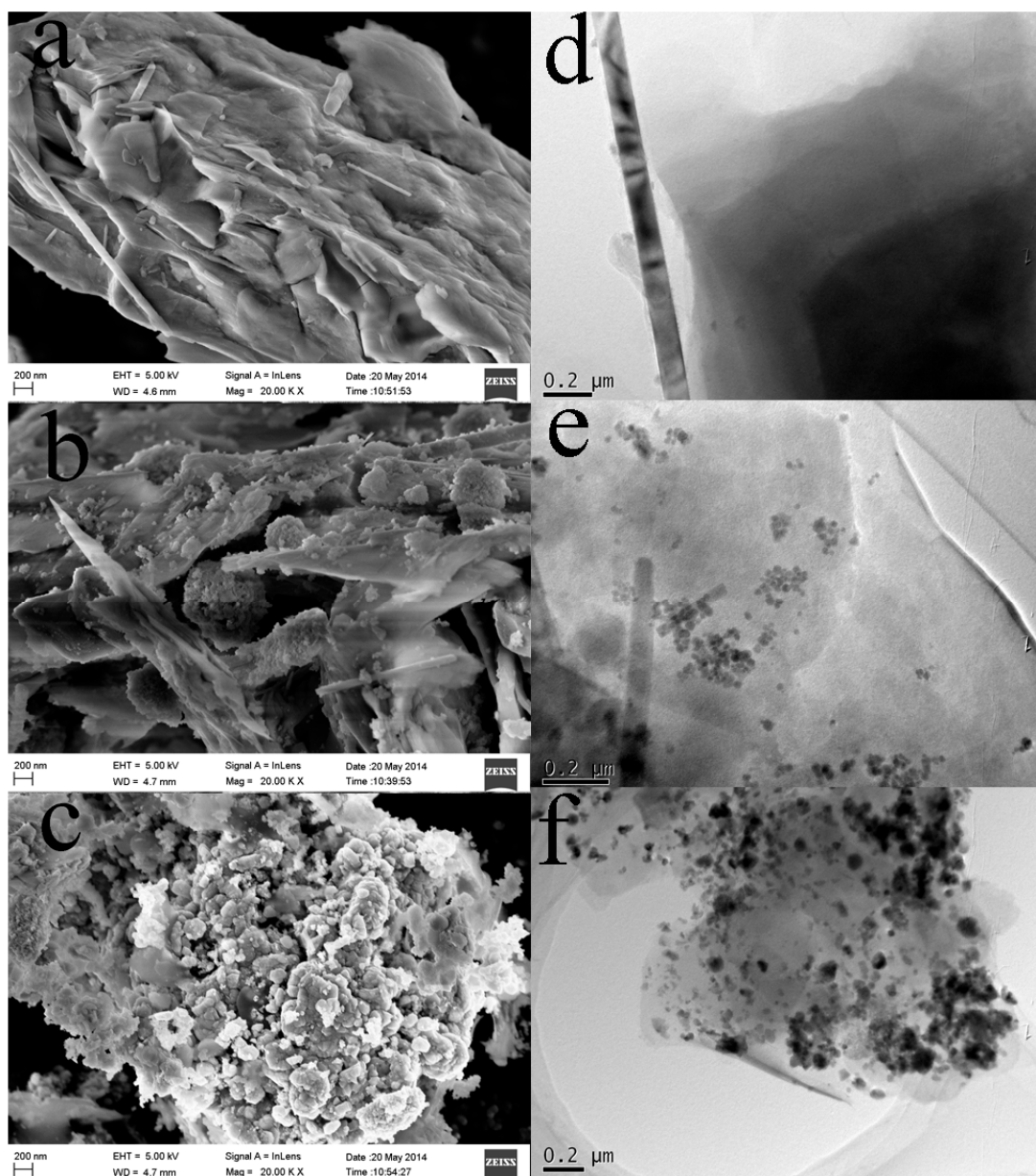
2.1. Morphology and BET Surface Area of the REC/ Fe_3O_4 / ZnO Composites

The morphologies of the various REC/ Fe_3O_4 / ZnO composites were investigated by SEM and TEM (Figure 1). REC is an interstratified clay mineral (Figure 1a,d). Breakage of the structure (Figure 1b) formed particles having diameters of ca. 6–35 nm (Figure 1e), in which Fe_3O_4 was integrated with the mineral. The structure became further disrupted with the deposition of ZnO (Figure 1c) when many more particles were found with the REC (Figure 1f).

BET surface area of REC applied in this study was $11.7 \text{ m}^2 \text{ g}^{-1}$ (Table 1), which is 25% smaller than that of REC/ Fe_3O_4 . The increase of BET after magnetization was mainly because of the breakage of REC as shown in Figure 1e. BET surface area was approximately 16.8 and 16.0 for REC/ ZnO and REC/ Fe_3O_4 / ZnO composites, respectively.

Table 1. Specific surface area of ZnO, REC, REC/Fe₃O₄ (1:0.3), REC/ZnO (1:0.5), REC/Fe₃O₄/ZnO (1:0.3:0.5) powder.

BET Surface Area (m ² ·g ⁻¹)	ZnO	REC	REC/Fe ₃ O ₄	REC/ZnO	ZnO/REC/Fe ₃ O ₄
	5.3	11.7	15.6	16.8	16.0

**Figure 1.** Scanning electron microscopy (SEM) images of (a) rectorite (REC), (b) REC/magnetite (Fe₃O₄) (1:0.3), and (c) REC/Fe₃O₄/zinc oxide (ZnO) (1:0.3:0.5) and transmission electron microscopy (TEM) images of (d) REC, (e) REC/Fe₃O₄ (1:0.3), and (f) REC/Fe₃O₄/ZnO (1:0.3:0.5).

2.2. Structural Characterization of the REC/Fe₃O₄/ZnO Composites

Figure 2 shows the XRD patterns of ZnO, REC and their composite materials for 2θ ranging from 10 to 70°. The diffraction peak at $2\theta = 19.8^\circ$ was a characterized peak of REC [52], which was also observed in REC/ZnO, REC/Fe₃O₄ and REC/Fe₃O₄/ZnO. The relative intensities of diffraction peak at $2\theta = 19.8^\circ$ was changed in composites, compared with that in pure REC. The finding indicates that

the structure of rectorite distorted to some extents during the synthesis of composites. Similar results were also reported during the synthesis of other REC-based photocatalyst [52]. Peaks observed at 31.7° , 34.4° , 36.2° , 47.5° , 56.5° , 62.8° , 66.3° , 67.9° , and 69.0° were indexed to hexagonal wurtzite (ZnO; JCPDS Data Card no. 36-1451). Diffraction peaks at 33.1° , 35.7° , 40.8° , 54.1° , and 64.0° , characteristic of Fe_3O_4 were observed for the REC/ Fe_3O_4 and REC/ Fe_3O_4 /ZnO composites [48]. The diameters of ZnO and Fe_3O_4 were approximately 45.7 and 22.4 nm in REC/ Fe_3O_4 /ZnO, putting diffraction peaks at $2\theta = 36.3^\circ$ and 19.8° and the corresponding FWHM (full width at half maxima) into Scherrer equation. The relative size between ZnO and Fe_3O_4 was correlated with that shown in Figure 1e,f.

Figure 3 compares the Fourier transform-infrared (FT-IR) spectra of REC and its composites. The spectra of REC, ZnO/REC, and REC/ Fe_3O_4 /ZnO were quite similar, with only small differences in band locations and intensities. The bands at 3645–3647 and 3429–3440 cm^{-1} were attributed to the hydrogen-bonding bending vibration of water and hydroxyl stretching vibration in all three samples [53]. Bands observed at 1635 and 1386 cm^{-1} in ZnO were attributed to the asymmetrical and symmetrical stretching of the zinc carboxylate [54], respectively. The band at 1635 cm^{-1} overlapped with the band at 1640 cm^{-1} , which was assigned to a water bending vibration in REC [55,56]. Bands at 1021 and 1053 cm^{-1} were assigned as In-plane Si–O–Si stretching [56], which was found to be 1012 and 1047 cm^{-1} in REC/ZnO and REC/ Fe_3O_4 /ZnO in this study. Bands at 478 and 545 cm^{-1} were assigned as Si–O bending and Si–O–Al bending [56], which was 486 and 548 cm^{-1} in REC/ZnO, and 490 and 552 cm^{-1} in REC/ Fe_3O_4 /ZnO, respectively. Notably, band at approximately 530–580 cm^{-1} was also reported to Fe–O bond [57] in Fe_3O_4 , which could be emerged in Si–O–Al bending band.

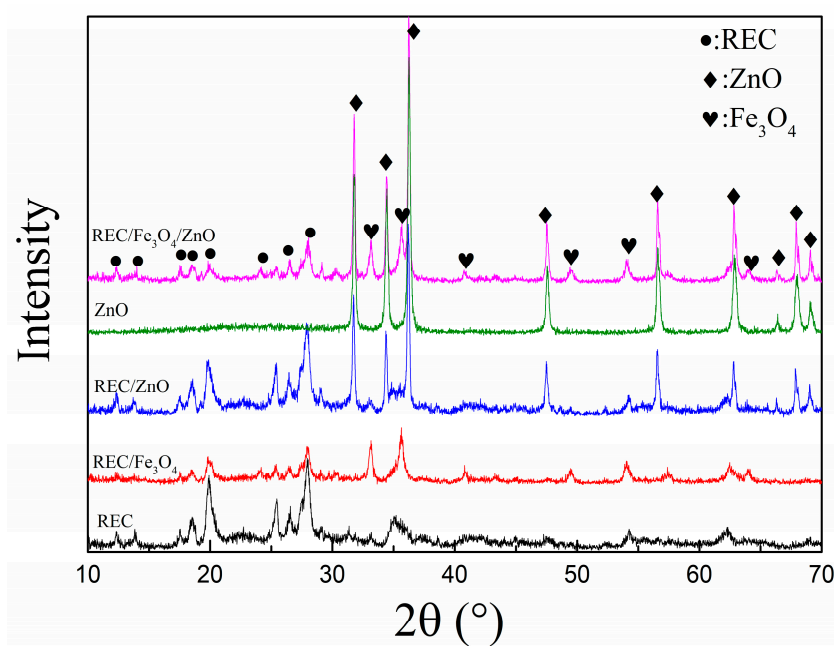


Figure 2. X-ray diffraction (XRD) patterns of REC, ZnO, REC/ZnO (1:0.5), REC/ Fe_3O_4 (1:0.3) and REC/ Fe_3O_4 /ZnO (1:0.3:0.5).

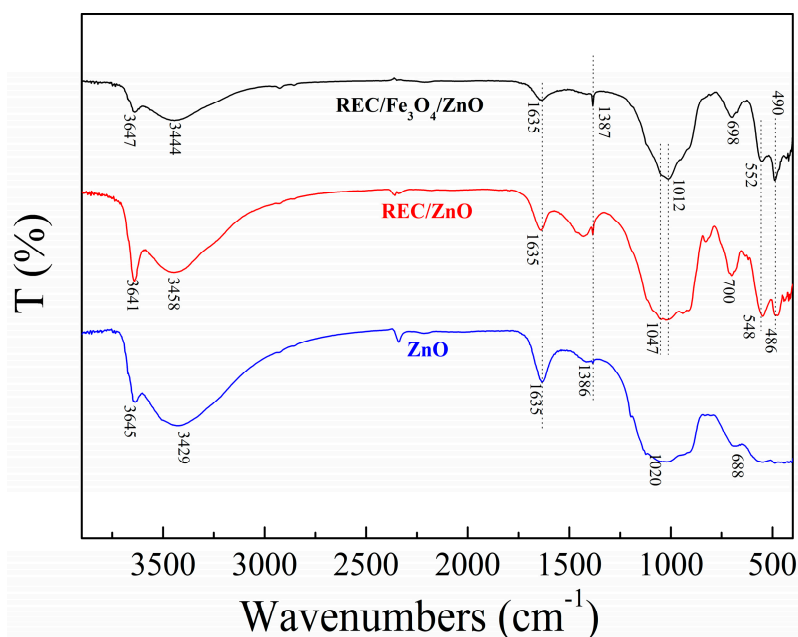


Figure 3. Fourier transform-infrared (FT-IR) spectra of ZnO, REC/ZnO (1:0.5), and ZnO/REC/Fe₃O₄ (1:0.3:0.5).

2.3. Thermogravimetric Analysis (TGA) Analysis REC and REC/Fe₃O₄/ZnO

TGA analysis was investigated to investigate the stability of ternary composite. As shown in Figure 4, REC barely lose its weight up to 800 °C mainly because of the loss of binding water. As for REC/Fe₃O₄/ZnO, the loss of weight could be divided into two regions. Loss of water could result in the loss weight below 200 °C. Decomposition of ZnCO₃·2Zn(OH)₂ impurity could lead to the loss of weight at approximately 600 °C.

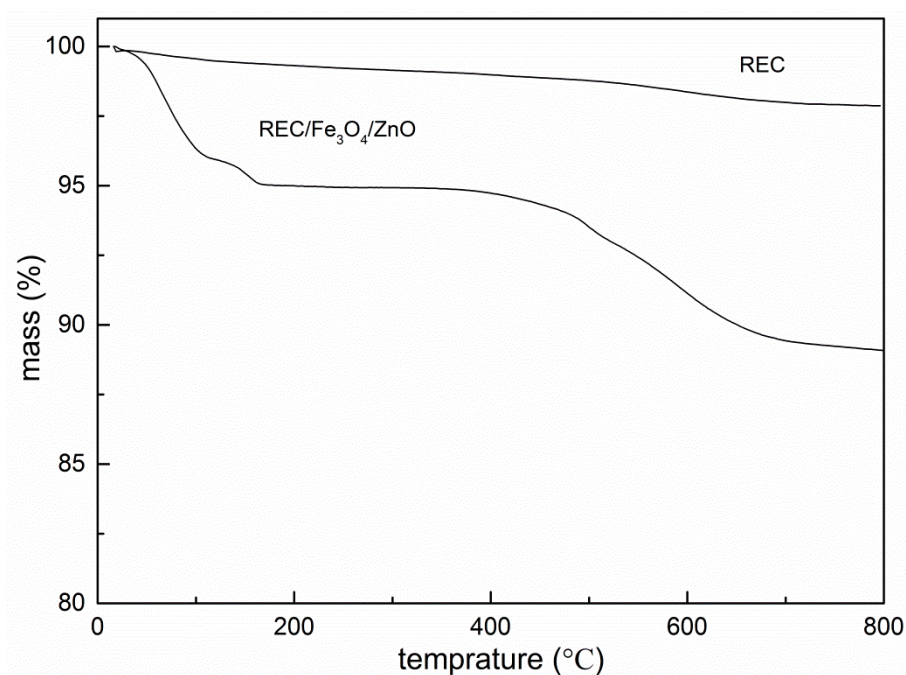


Figure 4. TGA of REC and REC/Fe₃O₄/ZnO (1:0.3:0.5).

2.4. Adsorption Equilibrium and Isotherm of MB Dye on REC/Fe₃O₄/ZnO

Figure 5a illustrates the results of equilibrium adsorption studies. The adsorption of MB dye increased with increasing time to 50 min, reaching equilibrium within 60 min for REC/Fe₃O₄/ZnO. The adsorption kinetics were fitted using different equations including pseudo-first-order, pseudo-second-order and Elovich models; the adjusted R -squared (adj. r^2) values were 0.98, 0.98, and 0.93, respectively. The calculated equilibrium adsorption was 1.5 and 2.2 mg/g from the pseudo-first-order and pseudo second-order models, respectively. The experimental equilibrium adsorption of 1.2 mg/g of MB dye on REC/Fe₃O₄/ZnO was thus consistent with pseudo-first-order kinetics.

The Freundlich and Langmuir isotherms are commonly used to describe the adsorption properties of pollutants. Figure 5b shows that the adsorption data fitted the Langmuir (adj. $r^2 = 0.999$) better than the Freundlich isotherm model (adj. $r^2 = 0.974$). The Langmuir isotherm is typically used to model monolayer adsorption on adsorbents having homogeneous and energetically uniform surfaces. Thus, our MB dye adsorption data are consistent with adsorption on the outer layer of the composites. The estimated recovered maximum adsorption capacity of MB dye on REC/Fe₃O₄/ZnO was 35.1 mg/g, which was 13% and 72% larger than that of REC/ZnO (31.1 mg/g) and ZnO (20.4 mg/g). These data clearly showed REC component contributed significantly to the adsorption of MB to REC/Fe₃O₄/ZnO.

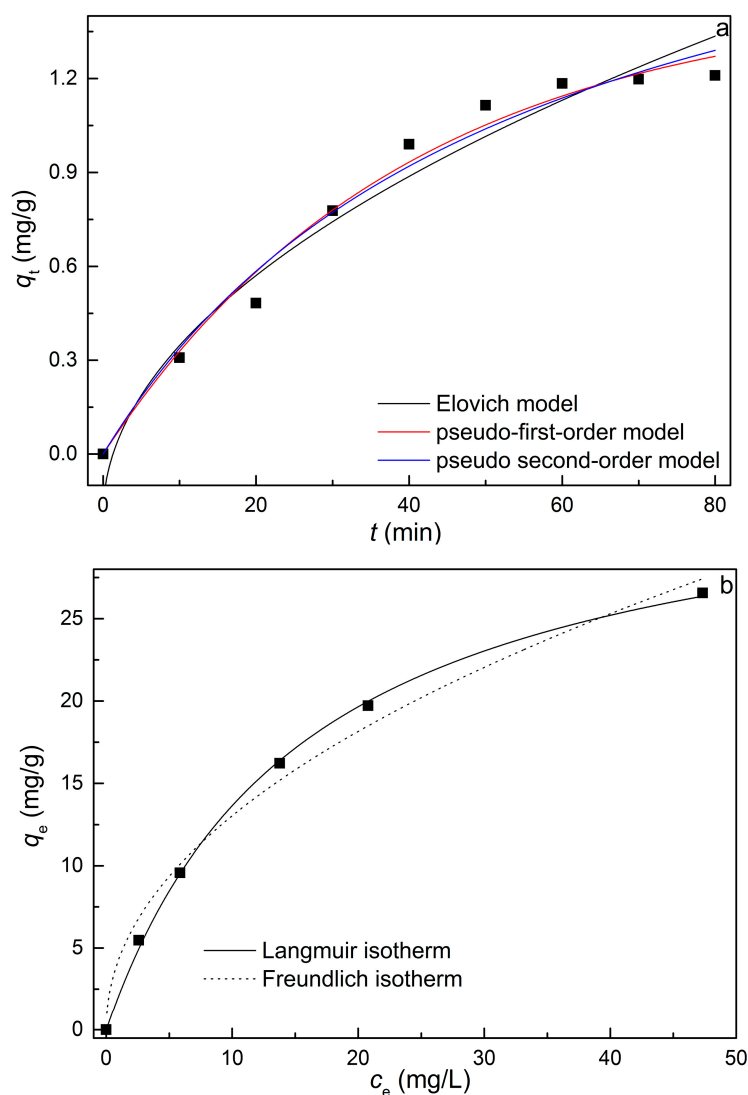


Figure 5. (a) Adsorption kinetics and (b) isotherm of methylene blue (MB) dye on REC/Fe₃O₄/ZnO (1:0.3:0.5).

2.5. Effect of Component Mass Ratio on the Degradation of MB Dye

The fabricated composites contained REC, Fe₃O₄, and ZnO. The impact of the component mass ratio on the removal of MB dye was investigated to obtain the optimal composition. Figure 6a shows that the dark adsorption of MB dye on REC/Fe₃O₄/ZnO was only slightly influenced by the ZnO content. After a 60-min adsorption period, the MB dye concentration in the bulk phase decreased to 4.2, 4.0, and 4.0 mg/L for ZnO contents of 1.5, 1.0, and 0.5, respectively. Control experiment showed that degradation of MB was negligible by direct photolysis in the absence of catalysts because of the low irradiance (1.9 mW/cm²). However, photodegradation of the MB dye was greatly influenced by the ZnO content, with the degradation clearly decreasing with increasing ZnO content. The observed degradation kinetic constant (k_{obs}) for the degradation of MB dye was 0.0056, 0.0086, and 0.012 min⁻¹ for ZnO contents of 1.5, 1.0, and 0.5, respectively. A plausible explanation for the decreased photoactivity with increasing ZnO content is that larger ZnO particles were formed, which may render the REC/Fe₃O₄/ZnO less photoactive.

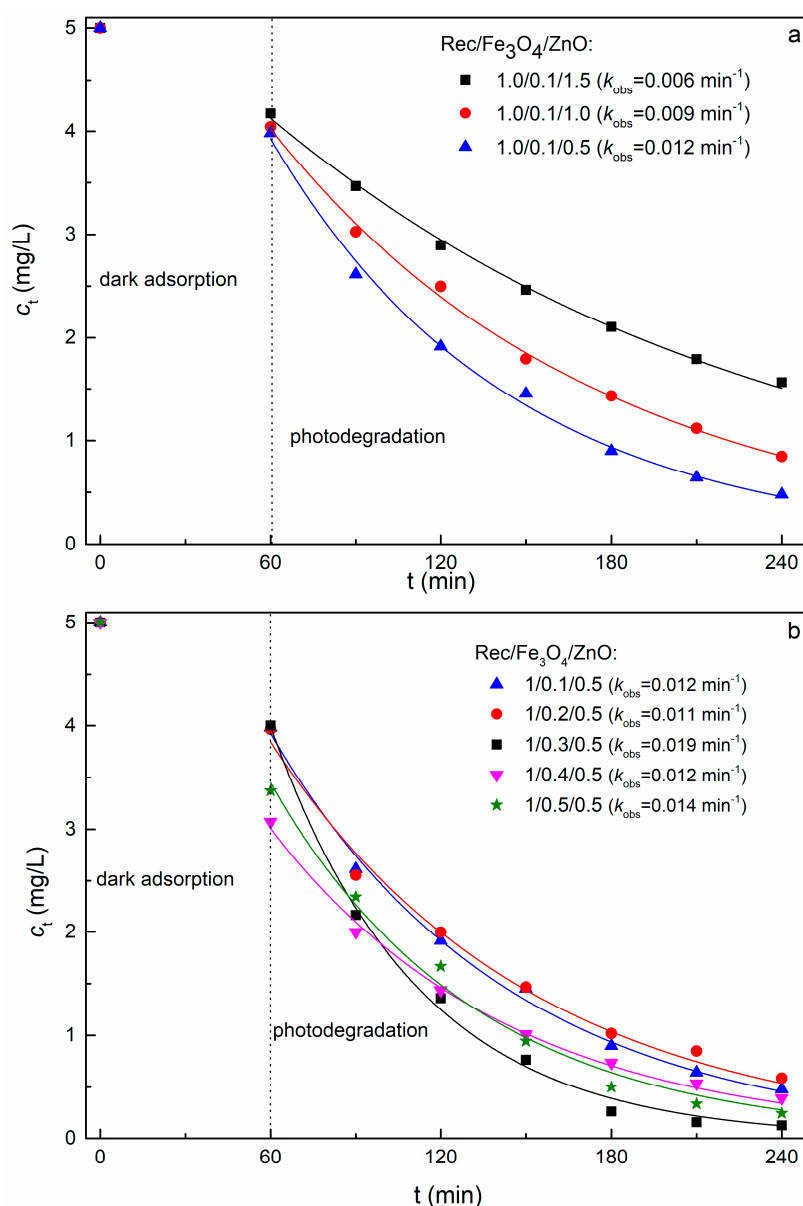


Figure 6. Effects of (a) ZnO and (b) Fe₃O₄ mass contents of REC/Fe₃O₄/ZnO on the adsorption and photodegradation of MB dye.

Figure 6b shows that the dark adsorption of MB dye was highly influenced by the Fe_3O_4 content of REC/ Fe_3O_4 /ZnO. The adsorption ratio first increased from 20 to 45% as the Fe_3O_4 content increased from 0.1 to 0.3; it then decreased to 33% as the Fe_3O_4 content increased to 0.5. However, k_{obs} for the MB photodegradation only slightly increased, from 0.012 to 0.015 min^{-1} , as the Fe_3O_4 content increased from 0.1 to 0.3, which indicated that the photodegradation was not significantly affected by the Fe_3O_4 content. Figure 1 shows that the layered structure of REC was damaged by the introduction of Fe_3O_4 , which was detrimental to MB dye adsorption. However, Fe_3O_4 was not an effective catalyst even under simulated solar radiation, particularly at neutral pH values. Therefore, the photoactivity of REC/ Fe_3O_4 /ZnO (as indicated by the degradation of adsorbed MB dye) was likely not greatly influenced by the Fe_3O_4 content. These results established that REC and ZnO acted mainly as adsorbent and photocatalyst, respectively, for the removal of MB dye by REC/ Fe_3O_4 /ZnO.

2.6. Effect of REC/ Fe_3O_4 /ZnO Dosage on the Degradation of MB Dye

Figure 7 shows that the dark adsorption of MB dye on REC/ Fe_3O_4 /ZnO slightly increased as the composite dosage increased from 0.3 to 1.1 g/L; this was attributed to increasing availability of adsorption sites. The photodegradation of MB dye also greatly increased with increasing dosage up to 0.9 g/L. The k_{obs} for the photodegradation of the MB dye increased from 0.0084 to 0.019 min^{-1} as the REC/ Fe_3O_4 /ZnO dosage increased from 0.3 to 0.9 g/L. These results are consistent with many studies where the reaction accelerates with increasing catalyst dosage when the amount of reactive species, such as $\bullet\text{OH}$, is determined by the concentration of the catalyst in the bulk solution. However, a dosage of 1.1 g/L had an inhibitory effect on the degradation of the dye. This was attributed to agglomeration of REC/ Fe_3O_4 /ZnO particles at the high concentration, which reduced light transmission. The optimal amount of added REC/ Fe_3O_4 /ZnO is the least amount required for complete photon absorption for the photodegradation reaction; in our experiments, we fixed the REC/ Fe_3O_4 /ZnO concentration at 0.9 g/L.

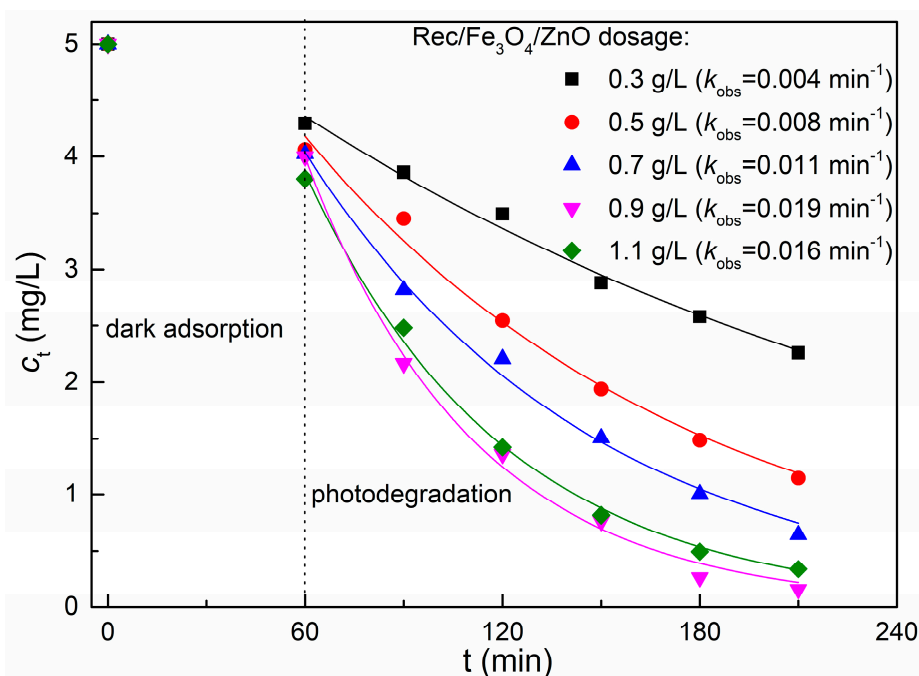


Figure 7. Effect of REC/ Fe_3O_4 /ZnO (1:0.3:0.5) dosage on the adsorption and photodegradation of MB dye.

2.7. Effect of Solution pH on the Degradation of MB Dye

The impact of solution pH on the adsorption and photodegradation of MB dye on REC/ Fe_3O_4 /ZnO is shown in Figure 8. It clearly shows that acidic solution favored the adsorption

of the dye and that the adsorption ratio at pH 5.0 was about twice that at other pH values. Conversely, degradation of the dye in acidic solution was much slower below pH 6.0. The rate constant k_{obs} increased from 0.011 to 0.019 min^{-1} as the solution pH increased from 5.0 to 6.0, and then decreased to 0.0076 min^{-1} at pH 8.0. These findings demonstrated that the solution pH had variable effect on the adsorption and degradation process of MB dye on REC/Fe₃O₄/ZnO. This variable effect of pH is related to its multiple roles in electrostatic interactions with the catalyst surface and substrate, and to the formation of charged radicals during the reaction process. This makes the interpretation of pH effects on the photodegradation of organic pollutants very difficult. The REC/Fe₃O₄/ZnO surface was negatively charged and the MB dye was present in its cationic form at pH 5.0. Therefore, the electrostatic attraction generated between cationic dye molecules and the negative surface charge contributed to the high adsorption ratio measured in acidic solutions. Typically, ZnO exhibits higher photoactivity at neutral pH. The degradation of MB dye on REC/Fe₃O₄/ZnO was faster at pH 6.0 because ZnO was the most important photocatalyst present in the composite at that pH.

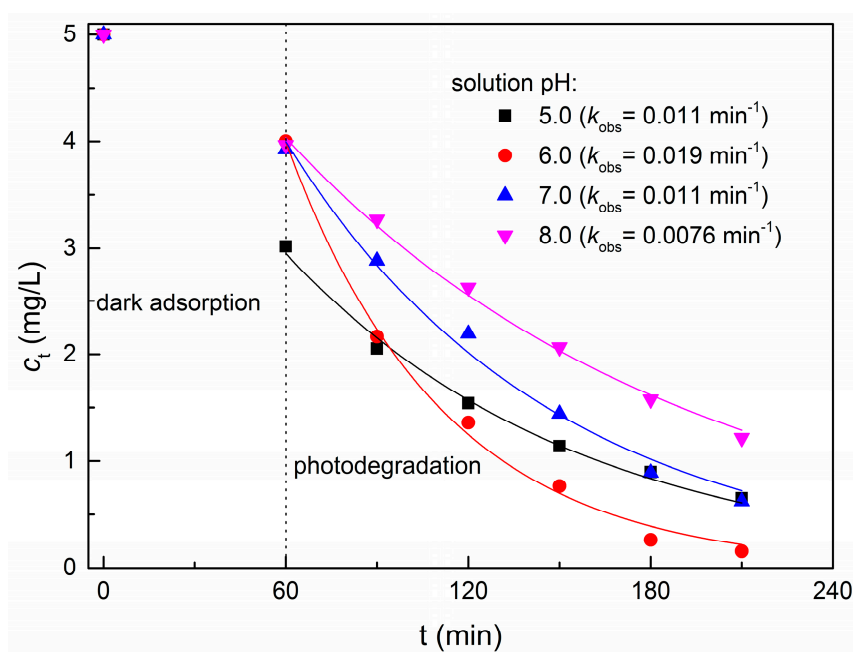


Figure 8. Effect of solution pH on the adsorption and photodegradation of MB dye on REC/Fe₃O₄/ZnO (1:0.3:0.5).

2.8. Kinetics for the Degradation of MB Dye on REC/Fe₃O₄/ZnO

The effect of initial MB dye concentration on its degradation was investigated for initial concentrations ranging from 5.0 to 30.0 mg/L (Figure 9a). After reaching adsorption equilibrium, the dye gradually decomposed with increasing irradiation time. The initial rate of photodegradation increased and reached a plateau with increasing initial dye concentration (Figure 9b). The data were fitted to the Langmuir–Hinshelwood kinetic model, which is frequently used to model the initial photocatalytic degradation rates of organic compounds. The rate law is given by Equation (1):

$$r_0 = -\frac{dc}{dt} = k_{re}K_s c_0 / (1 + K_s c_0), \quad (1)$$

where r_0 is the initial rate of disappearance of MB dye, c_0 is the initial concentration of the dye, k_{re} is the reaction rate constant, and K_s is the Langmuir adsorption constant. The calculated values for k_{re} and K_s were 0.122 mg/(L·min) and 0.069 L/mg, respectively.

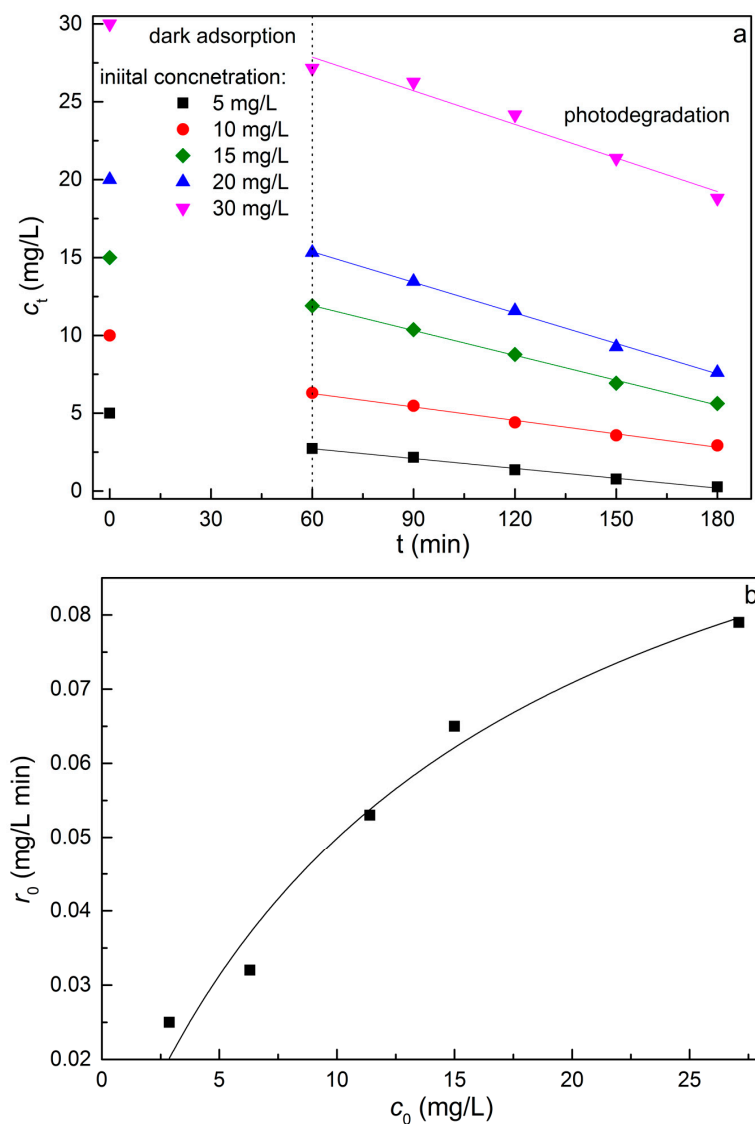


Figure 9. (a) Correlation between the initial rate of loss of MB dye on REC/Fe₃O₄/ZnO (1:0.3:0.5) and the initial dye concentration. (b) The solid line represents fitting of the data to the Langmuir–Hinshelwood kinetic model.

2.9. Recovery and Stability of REC/Fe₃O₄/ZnO

The performance of a single catalyst sample for the removal of MB dye over several cycles was determined to assess the photostability and possible reuse of REC/Fe₃O₄/ZnO. After 1-h adsorption and 5-h irradiation sequences, the composite was recovered from the reaction solution using an external magnet and redispersed in fresh 5-mg/L MB dye solution. Figure 10 shows that a noticeable decrease in the removal ratio of the dye occurred during repeated use of the REC/Fe₃O₄/ZnO catalyst. Only 80% remained after three cycles, corresponding to a mass loss of 14%. The results demonstrated satisfactory photostability of the REC/Fe₃O₄/ZnO catalyst.

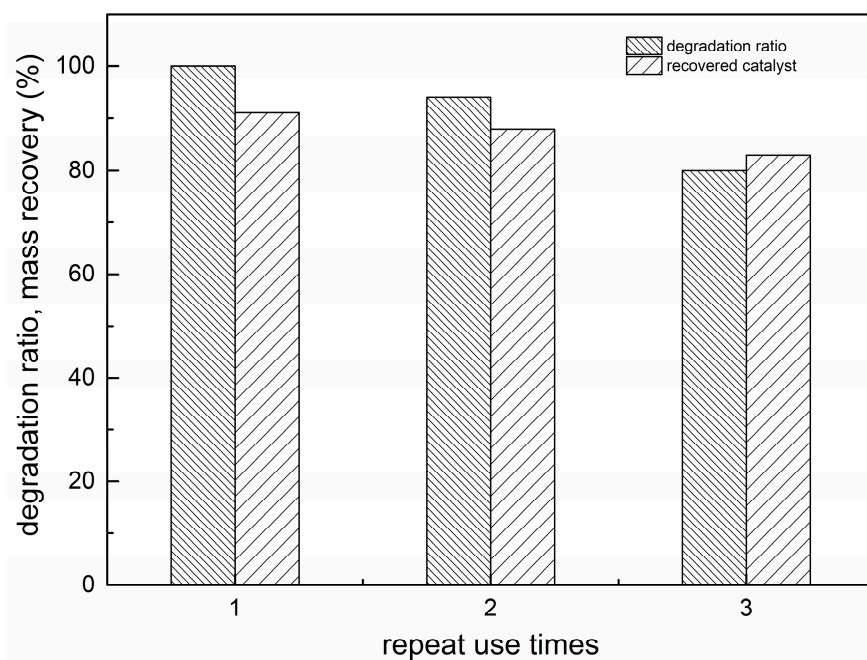
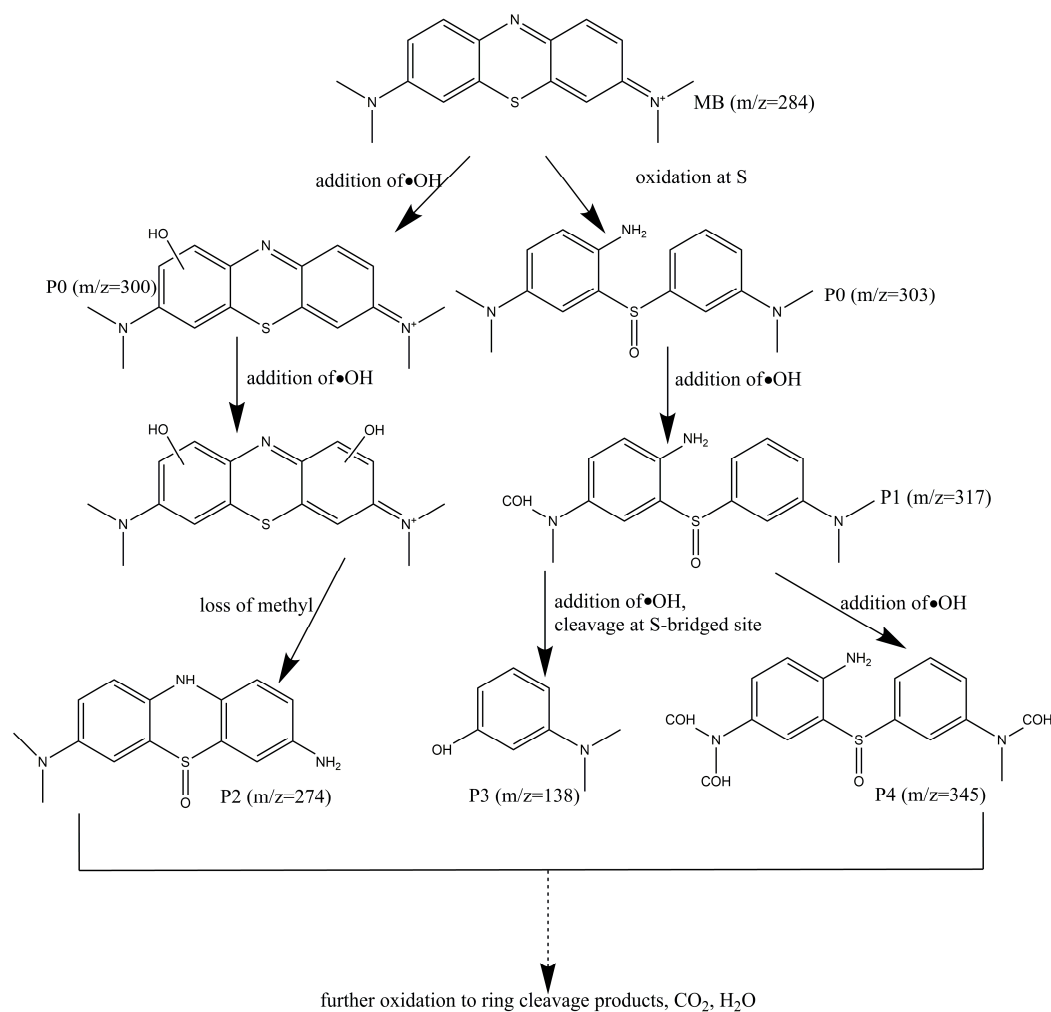


Figure 10. Performance and recovery of REC/Fe₃O₄/ZnO (1:0.3:0.5) during repeated use.

2.10. Mechanism for the Degradation of MB Dye on REC/Fe₃O₄/ZnO

The degradation intermediates were identified by liquid chromatography-mass spectrometry (LC-MS). The signal at $m/z = 284$ present before degradation was assigned to the MB dye molecule (Scheme 1). Oxidation of MB dye could follow different paths. Addition of $\bullet\text{OH}$ to MB dye molecules would lead to the formation of an intermediate with $m/z = 300$ [58]. Oxidation of sulfur atoms and bond cleavage at nitrogen-bridged sites would lead to the formation of a sulfoxide intermediate having $m/z = 303$ [59]. However, neither $m/z = 300$ nor 303 was detected in the present study. Instead, signals were found at $m/z = 317, 274, 138,$ and 345. An intermediate with $m/z = 317$ could be formed through the addition of two $\bullet\text{OH}$ radicals per MB dye molecule, or through oxidation of methyl ($-\text{CH}_3$) groups of the sulfoxide intermediate, and the oxidation of more methyl groups would lead to the formation of a species having $m/z = 345$. Addition of $\bullet\text{OH}$ to an intermediate of $m/z = 317$ and cleavage at a sulfur-bridged site might lead to the formation of an intermediate with $m/z = 138$. Additionally, loss of a methyl group could produce an intermediate with $m/z = 274$. Contribution of $\bullet\text{OH}$ to the degradation of MB was proved by a much smaller degradation kinetic constant in the presence of isopropanol acting as $\bullet\text{OH}$ scavenger. Oxidation of these intermediates could form ring cleavage products, and even mineralization to CO_2 and H_2O is plausible. The chemical structures of any intermediates were not identified because of the complexity of the degradation process.



Scheme 1. Proposed pathway for the degradation of MB dye on REC/Fe₃O₄/ZnO (1:0.3:0.5).

3. Materials and Methods

3.1. Chemicals

Ferric chloride, ferric sulfate, MB, zinc acetate dihydrate (Zn(CH₃COO)₂·2H₂O) (purity: 99.9%), hydrazine hydrate, dimethyl benzene, ethylene glycol, ethyl alcohol, and sodium hydroxide were purchased from Alpha-Aesar (Shanghai, China) and used as-received. They were of analytical grade. Refined REC was provided by Hubei Mingliu Inc. Co. (Wuhan, China). The water used in the experiments had been pretreated with an ultrapure water system (Liyuan Electric Instrument Co., Beijing, China).

3.2. Synthesis of REC/Fe₃O₄/ZnO

3.2.1. Synthesis of Magnetic REC

Fe₃O₄ was prepared by a co-precipitation method as follows. A solution of FeCl₃ (1.625 g) and FeSO₄ (1.219 g) was prepared at a molar ratio of 4:3, and 1 mol/L of NaOH solution (250 mL) was quickly added to the mixture while mixing at high speed with a magnetic mixer to adjust the pH to 11. Mixing was continued at 60 °C for 1.5 h, and then the solution was placed in a thermostated water bath at 80 °C for 1.5 h to crystallize the product. The Fe₃O₄ product was isolated by filtration, rinsed with pure water until the pH of the filtrate was neutral, dried at 105 °C for 6 h, and finally ground to a particle size of 74 μm.

Magnetic REC was prepared as follows. A mixture of REC in water was sonicated to provide a uniform suspension. A ferrofluid containing 50 wt. % of the Fe_3O_4 described above was slowly dropped into REC suspensions to provide REC/ Fe_3O_4 mixtures having weight ratios of 1:0.1, 1:0.2, 1:0.3, 1:0.4, and 1:0.5. Each mixture was ultrasonically dispersed for 60 min. The product was recovered by filtration, dried at 105 °C for 6 h, and ground to a particle size of 74 μm .

3.2.2. Synthesis of REC/ Fe_3O_4 /ZnO

The REC/ Fe_3O_4 /ZnO nanocomposites were prepared via a mild liquid-phase synthesis method. The reaction of zinc acetate dihydrate ($\text{Zn}(\text{CH}_3\text{COO})_2 \cdot 2\text{H}_2\text{O}$; 2.1951 g (10 mmol)) with hydrazine hydrate ($\text{N}_2\text{H}_4 \cdot \text{H}_2\text{O}$; 80%; 0.726 mL (15 mmol)) provided a theoretical yield of 0.8137 g of ZnO. Based on this calculation, appropriate amounts of the magnetic REC were added to form REC/ Fe_3O_4 /ZnO suspensions having weight ratios of 1:0.1:0.5, 1:0.2:0.5, 1:0.3:0.5, 1:0.4:0.5, 1:0.5:0.5, 1:0.1:1.0 and 1:0.1:1.5. In the experiments, 2.1951 g (10 mmol) of $\text{Zn}(\text{CH}_3\text{COO})_2 \cdot 2\text{H}_2\text{O}$ and the appropriate calculated weights of magnetic REC were dissolved in 200 mL of a mixed solvent of dimethyl benzene and ethylene glycol under vigorous stirring for 30 min. Then, a solution of hydrazine hydrate (0.726 mL, 15 mmol) in anhydrous ethanol (30 mL) was added dropwise to the suspension. The resulting dispersion was vigorously stirred for 5 h at room temperature, and then transferred to a separating funnel and allowed to stand for 1.5 h. Centrifugation provided the REC/ Fe_3O_4 /ZnO nanocomposites as gray solids. These were isolated by filtration, rinsed three times with anhydrous ethanol, and calcined for 6 h in a muffle furnace at temperatures of 200, 300, 400, 500, and 600 °C.

3.3. Characterization of the Synthesized Magnetic Materials

The Brunauer–Emmett–Teller (BET) surface area was determined using a Micromeritics model ASAP 2020 Instrument (Micromeritics, Norcross, GA, USA). The XRD patterns of the products were determined using a Dmax-rA powder diffractometer (Rigaku, Akishima, Japan), which used $\text{Cu K}\alpha$ radiation source at a scanning rate of 2° min^{-1} . SEM images were acquired using a QUANTA 200 instrument (FEI, Hillsboro, OR, USA). Transmission electron microscopy (TEM) images were obtained with a JEM 2010HT instrument (JEOL, Akishima, Japan) at an accelerating voltage of 200 kV. Thermogravimetric analysis (TGA) was conducted on a TGA 2050 thermogravimetric analyzer with a heating rate of $10^\circ \text{C}/\text{min}$ from 50 to 800 °C under a nitrogen atmosphere (TA Instruments, NewCastle, DE, USA). The Brunauer–Emmett–Teller (BET) surface areas of the two TiO_2 were determined using a Micromeritics ASAP 2020 setup (Micromeritics, Norcross, GA, USA).

3.4. Adsorption of MB Dye on REC/ Fe_3O_4 /ZnO

Adsorption kinetics: A dispersion of REC/ Fe_3O_4 /ZnO (0.9 g/L) was prepared by adding REC/ Fe_3O_4 /ZnO to 100 mL of an aqueous MB solution (concentration: 5 mg/L) and the dispersion was shaken at 25 °C. Samples (2 mL) were withdrawn from the flask at different time intervals. The adsorbent and MB dye solution were quickly separated by a magnet, and the concentration of dye in the supernatant was analyzed by UV-visible spectroscopy.

Adsorption isotherms: Batch adsorption studies were performed using aqueous suspensions containing MB dye at different initial concentrations; the dosage of REC/ Fe_3O_4 /ZnO, REC/ Fe_3O_4 or ZnO as adsorbent was held at 0.9 g/L. The suspension was continuously stirred at constant temperature using a mechanical stirrer for 2 h. After reaching equilibrium, a 2-mL aliquot of the suspension was withdrawn to determine the equilibrium concentration, c_t . Adsorption isotherm experiments were carried out at pH 6.0 in the absence of electrolytes.

3.5. Photocatalytic Degradation of MB Dye under Simulated Solar Radiation

Photodegradation of MB dye was carried out in a home-made photoreactor. The radiation source was an incandescent light bulb lamp that provided radiation at $\geq 350 \text{ nm}$ with an irradiance of $1900 \mu\text{W}/\text{cm}^2$ (Figure 11). Aqueous solutions of MB dye (200 mL; initial concentration: 5 to 20 mg/L)

were mixed magnetically with the various catalysts in a 250 mL Pyrex beaker. After equilibrating in the dark for 1 h, aliquots (2 mL) of those suspensions were withdrawn to determine the initial MB concentration, c_0 . Aliquots (2 mL) were also collected at selected time intervals as the MB degraded; these were magnetically separated and used to determine c_t . The degradation of the MB dye was monitored using a 2550 UV-visible spectrophotometer (Shimadzu, Kyoto, Japan) with a 10-mm cuvette. The slope of a linear fit of the data provided the initial photodegradation rate, R_0 .

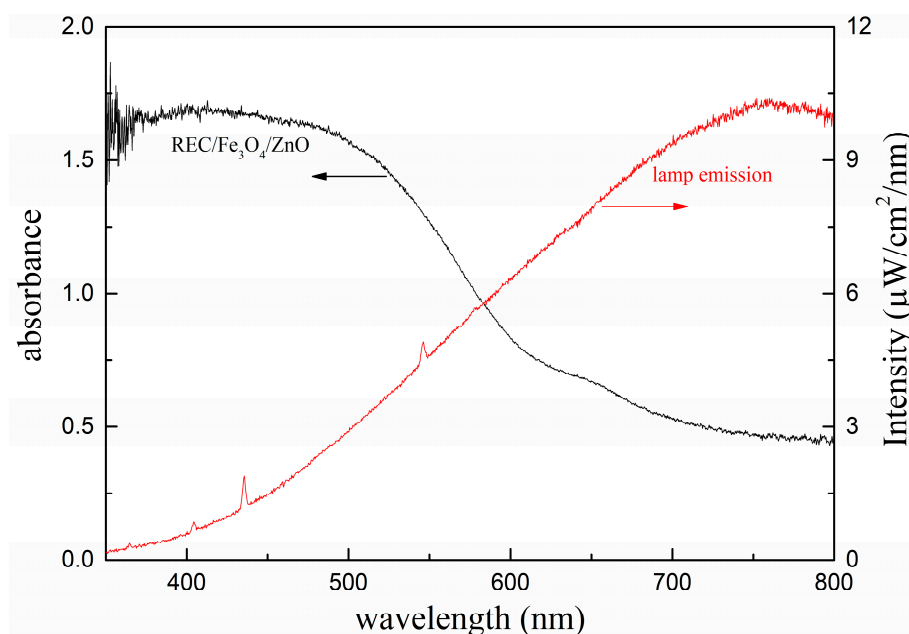


Figure 11. Absorption spectrum of REC/Fe₃O₄/ZnO (1:0.3:0.5) and the irradiance of lamp using in this study.

3.6. Sample and Data Analyses

Sample analysis: The MB dye concentration was determined according to its absorbance at 665 nm.

Data analysis: The mass of MB dye adsorbed per gram of adsorbent at different times (q_t , mg/g) and at equilibrium (q_e , mg/g) were calculated using Equations (2) and (3), respectively:

$$q_t = \frac{(c_0 - c_t) \times V}{m}, \quad (2)$$

$$q_e = \frac{(c_0 - c_e) \times V}{m}, \quad (3)$$

where c_0 , c_t , and c_e are the initial concentration, concentration at time t , and equilibrium concentration of the MB dye (all in mg/g), respectively.

The adsorption ratio (%) of the MB dye was then calculated using Equation (4):

$$R = \left(1 - \frac{c_e}{c_0}\right) \times 100\%, \quad (4)$$

The Freundlich (Equation (5)) and Langmuir (Equation (6)) isotherms were applied to describe the adsorption properties of the MB dye on REC/Fe₃O₄/ZnO, REC/Fe₃O₄ and ZnO, as follows [60]:

$$q_e = K_F \times c_e^{1/n}, \quad (5)$$

where K_F ($(\text{mg/g}) \times (\text{L/g})^{1/n}$) is the Freundlich affinity coefficient and $1/n$ is the Freundlich exponential coefficient. Additionally:

$$q_e = \frac{q_{\max} \times K_L \times c_e}{1 + K_L \times c_e}, \quad (6)$$

where q_{\max} (mg/g) is the maximum adsorption of MB dye on the adsorbents and K_L (L/mg) is the Langmuir adsorption constant.

4. Conclusions

A series of REC/Fe₃O₄/ZnO composites was synthesized and characterized. The Fe₃O₄ phase destroyed the layered structure of REC and increased the adsorption of MB dye. The ZnO component greatly assisted the degradation of the dye, with the activity of REC/Fe₃O₄/ZnO decreasing with increasing ZnO content. REC/Fe₃O₄/ZnO exhibited the highest photoactivity for the removal of MB dye at pH 6.0. The adsorption isotherm and degradation kinetics followed the Langmuir and Langmuir–Hinshelwood models, respectively. The mass loss and photoactivity of REC/Fe₃O₄/ZnO only slightly decreased after three cycles. The primary degradation mechanism was also proposed based on the detected intermediates. Our study demonstrated that REC/Fe₃O₄/ZnO composites have great potential as catalysts for the treatment of dye pollutants in aqueous solutions.

Acknowledgments: This research is supported by the National High Technology Research and Development Program of China (No. 2007AA06Z418), the National Natural Science Foundation of China (Nos. 20577036, 20777058, 20977070), the National Natural Science Foundation of Hubei province in China (No. 2015CFA137), and the Open Fund of Hubei Biomass-Resource Chemistry and Environmental Biotechnology Key Laboratory, and the Fund of Eco-environment Technology R&D and Service Center (Wuhan University).

Author Contributions: Peijiang Zhou and Huanhuan Wang conceived and designed the experiments; Rui Guo, Yifei Wang and Yunfei Yuan performed the experiments; Huanhuan Wang and Hongju Zhan analyzed the data; Peijiang Zhou contributed reagents/materials/analysis tools; Huanhuan Wang wrote the paper.

Conflicts of Interest: The authors declare no conflict of interest.

References

1. Forgacs, E.; Cserhati, T.; Oros, G. Removal of synthetic dyes from wastewaters: A review. *Environ. Int.* **2004**, *30*, 953–971. [[CrossRef](#)] [[PubMed](#)]
2. An, A.K.; Guo, J.; Lee, E.J.; Jeong, S.; Zhao, Y.; Wang, Z.; Leiknes, T. PDMS/PVDF hybrid electrospun membrane with superhydrophobic property and drop impact dynamics for dyeing wastewater treatment using membrane distillation. *J. Membr. Sci.* **2017**, *525*, 57–67. [[CrossRef](#)]
3. Zinatloo-Ajabshir, S.; Salavati-Niasari, M.; Zinatloo-Ajabshir, Z. Facile size-controlled preparation of highly photocatalytically active praseodymium zirconate nanostructures for degradation and removal of organic pollutants. *Sep. Purif. Technol.* **2017**, *177*, 110–120. [[CrossRef](#)]
4. Giannakoudakis, D.A.; Kyzas, G.Z.; Avranas, A.; Lazaridis, N.K. Multi-parametric adsorption effects of the reactive dye removal with commercial activated carbons. *J. Mol. Liq.* **2016**, *213*, 381–389. [[CrossRef](#)]
5. Spagnoli, A.A.; Giannakoudakis, D.A.; Bashkova, S. Adsorption of methylene blue on cashew nut shell based carbons activated with zinc chloride: The role of surface and structural parameters. *J. Mol. Liq.* **2017**, *229*, 465–471. [[CrossRef](#)]
6. Chang, S.H.; Wang, K.S.; Chao, S.J.; Peng, T.H.; Huang, L.C. Degradation of azo and anthraquinone dyes by a low-cost Fe⁰/air process. *J. Hazard. Mater.* **2009**, *166*, 1127–1133. [[CrossRef](#)] [[PubMed](#)]
7. Ganesh, R.; Boardman, G.D.; Michelsen, D. Fate of azo dyes in sludges. *Water Res.* **1994**, *28*, 1367–1376. [[CrossRef](#)]
8. Razo-Flores, E.; Luijten, M.; Donlon, B.; Lettinga, G.; Field, J. Biodegradation of selected azo dyes under methanogenic conditions. *Water Sci. Technol.* **1997**, *36*, 65–72.
9. Lucas, M.; Peres, J. Decolorization of the azo dye reactive black 5 by Fenton and photo-Fenton oxidation. *Dyes Pigment.* **2006**, *71*, 236–244. [[CrossRef](#)]

10. Zhang, X.; Wang, Y.; Liu, B.; Sang, Y.; Liu, H. Heterostructures construction on TiO₂ nanobelts: A powerful tool for building high-performance photocatalysts. *Appl. Catal. B Environ.* **2017**, *202*, 620–641. [[CrossRef](#)]
11. Tan, C.; Cao, X.; Wu, X.J.; He, Q.; Yang, J.; Zhang, X.; Chen, J.; Zhao, W.; Han, S.; Nam, G.H.; et al. Recent advances in ultrathin two-dimensional nanomaterials. *Chem. Rev.* **2017**, *117*, 6225–6331. [[CrossRef](#)] [[PubMed](#)]
12. Pirhashemi, M.; Habibi-Yangjeh, A. Ultrasonic-assisted preparation of plasmonic ZnO/Ag/Ag₂WO₄ nanocomposites with high visible-light photocatalytic performance for degradation of organic pollutants. *J. Colloid Interface Sci.* **2017**, *491*, 216–229. [[CrossRef](#)] [[PubMed](#)]
13. Karunakaran, C.; Dhanalakshmi, R. Photocatalytic performance of particulate semiconductors under natural sunshine—Oxidation of carboxylic acids. *Sol. Energy Mater. Sol. Cells* **2008**, *92*, 588–593. [[CrossRef](#)]
14. Madhavan, J.; Muthuraaman, B.; Murugesan, S.; Anandan, S.; Maruthamuthu, P. Peroxomonosulphate, an efficient oxidant for the photocatalysed degradation of a textile dye, acid red 88. *Sol. Energy Mater. Sol. Cells* **2006**, *90*, 1875–1887. [[CrossRef](#)]
15. Kumar, S.; Karthikeyan, S.; Lee, A. G-C₃N₄-based nanomaterials for visible light-driven photocatalysis. *Catalysts* **2018**, *8*, 74. [[CrossRef](#)]
16. Jelle, A.A.; Hmadeh, M.; O'Brien, P.G.; Perovic, D.D.; Ozin, G.A. Photocatalytic properties of all four polymorphs of nanostructured iron oxyhydroxides. *ChemNanoMat* **2016**, *2*, 1047–1054. [[CrossRef](#)]
17. Zhang, G.; Lan, Z.A.; Wang, X. Conjugated polymers: Catalysts for photocatalytic hydrogen evolution. *Angew. Chem.-Int. Ed.* **2016**, *55*, 15712–15727. [[CrossRef](#)] [[PubMed](#)]
18. Zhang, L.; Li, J.; Chen, Z.; Tang, Y.; Yu, Y. Preparation of fenton reagent with H₂O₂ generated by solar light-illuminated nano-Cu₂O/MWNTs composites. *Appl. Catal. A Gen.* **2006**, *299*, 292–297. [[CrossRef](#)]
19. Ali, I.; Kim, J.O. Continuous-flow photocatalytic degradation of organics using modified TiO₂ nanocomposites. *Catalysts* **2018**, *8*, 43. [[CrossRef](#)]
20. Ho, W.; Tay, Q.; Qi, H.; Huang, Z.; Li, J.; Chen, Z. Photocatalytic and adsorption performances of faceted cuprous oxide (Cu₂O) particles for the removal of methyl orange (MO) from aqueous media. *Molecules* **2017**, *22*, 677. [[CrossRef](#)] [[PubMed](#)]
21. Mohd Hir, Z.; Abdullah, A.; Zainal, Z.; Lim, H. Photoactive hybrid film photocatalyst of polyethersulfone-ZnO for the degradation of methyl orange dye: Kinetic study and operational parameters. *Catalysts* **2017**, *7*, 313. [[CrossRef](#)]
22. Shu, H.Y.; Chang, M.C.; Tseng, T.H. Solar and visible light illumination on immobilized nano zinc oxide for the degradation and mineralization of orange G in wastewater. *Catalysts* **2017**, *7*, 164.
23. Sharma, D.; Sharma, S.; Kaith, B.S.; Rajput, J.; Kaur, M. Synthesis of zno nanoparticles using surfactant free in-air and microwave method. *Appl. Surf. Sci.* **2011**, *257*, 9661–9672. [[CrossRef](#)]
24. Giannakoudakis, D.A.; Arcibar-Orozco, J.A.; Bandosz, T.J. Key role of terminal hydroxyl groups and visible light in the reactive adsorption/catalytic conversion of mustard gas surrogate on zinc (hydr)oxides. *Appl. Catal. B Environ.* **2015**, *174–175*, 96–104. [[CrossRef](#)]
25. Ullah, R.; Dutta, J. Photocatalytic degradation of organic dyes with manganese-doped zno nanoparticles. *J. Hazard. Mater.* **2008**, *156*, 194–200. [[CrossRef](#)] [[PubMed](#)]
26. Chava, R.K.; Im, Y.; Kang, M. Nitrogen doped carbon quantum dots as a green luminescent sensitizer to functionalize zno nanoparticles for enhanced photovoltaic conversion devices. *Mater. Res. Bull.* **2017**, *94*, 399–407. [[CrossRef](#)]
27. He, W.; Jia, H.; Cai, J.; Han, X.; Zheng, Z.; Wamer, W.G.; Yin, J.-J. Production of reactive oxygen species and electrons from photoexcited zno and zns nanoparticles: A comparative study for unraveling their distinct photocatalytic activities. *J. Phys. Chem. C* **2016**, *120*, 3187–3195. [[CrossRef](#)]
28. Lakshmi Prasanna, V.; Vijayaraghavan, R. Insight into the mechanism of antibacterial activity of zno: Surface defects mediated reactive oxygen species even in the dark. *Langmuir ACS J. Surf. Colloids* **2015**, *31*, 9155–9162. [[CrossRef](#)] [[PubMed](#)]
29. Sun, L.; Shao, R.; Chen, Z.; Tang, L.; Dai, Y.; Ding, J. Alkali-dependent synthesis of flower-like zno structures with enhanced photocatalytic activity via a facile hydrothermal method. *Appl. Surf. Sci.* **2012**, *258*, 5455–5461. [[CrossRef](#)]
30. Mahmoodi, V.; Bastami, T.R.; Ahmadpour, A. Solar energy harvesting by magnetic-semiconductor nanoheterostructure in water treatment technology. *Environ. Sci. Pollut. Res. Int.* **2018**. [[CrossRef](#)] [[PubMed](#)]

31. Riahi-Madvaar, R.; Taher, M.A.; Fazelirad, H. Synthesis and characterization of magnetic halloysite-iron oxide nanocomposite and its application for naphthol green B removal. *Appl. Clay Sci.* **2017**, *137*, 101–106. [[CrossRef](#)]
32. Middea, A.; Spinelli, L.S.; Souza, F.G., Jr.; Neumann, R.; Fernandes, T.L.A.P.; Gomes, O.D.F.M. Preparation and characterization of an organo-palygorskite-Fe₃O₄ nanomaterial for removal of anionic dyes from wastewater. *Appl. Clay Sci.* **2017**, *139*, 45–53. [[CrossRef](#)]
33. Mu, B.; Tang, J.; Zhang, L.; Wang, A. Preparation, characterization and application on dye adsorption of a well-defined two-dimensional superparamagnetic clay/polyaniline/Fe₃O₄ nanocomposite. *Appl. Clay Sci.* **2016**, *132–133*, 7–16. [[CrossRef](#)]
34. Chang, J.; Ma, J.; Ma, Q.; Zhang, D.; Qiao, N.; Hu, M.; Ma, H. Adsorption of methylene blue onto Fe₃O₄/activated montmorillonite nanocomposite. *Appl. Clay Sci.* **2016**, *119*, 132–140. [[CrossRef](#)]
35. Hu, L.; Tang, X.; Wu, Z.; Lin, L.; Xu, J.; Xu, N.; Dai, B. Magnetic lignin-derived carbonaceous catalyst for the dehydration of fructose into 5-hydroxymethylfurfural in dimethylsulfoxide. *Chem. Eng. J.* **2015**, *263*, 299–308. [[CrossRef](#)]
36. Nur'aeni; Chae, A.; Jo, S.; Choi, Y.; Park, B.; Park, S.Y.; In, I. Synthesis of β-FeOOH/Fe₃O₄ hybrid photocatalyst using catechol-quaternized poly(N-vinyl pyrrolidone) as a double-sided molecular tape. *J. Mater. Sci.* **2017**, *52*, 8493–8501.
37. Shi, Z.; Yang, X.; Yao, S. Photocatalytic activity of cerium-doped mesoporous TiO₂ coated Fe₃O₄ magnetic composite under uv and visible light. *J. Rare Earths* **2012**, *30*, 355–360. [[CrossRef](#)]
38. Shekofteh-Gohari, M.; Habibi-Yangjeh, A. Novel magnetically separable Fe₃O₄@ZnO/AgCl nanocomposites with highly enhanced photocatalytic activities under visible-light irradiation. *Sep. Purif. Technol.* **2015**, *147*, 194–202. [[CrossRef](#)]
39. Majidnia, Z.; Idris, A. Combination of maghemite and titanium oxide nanoparticles in polyvinyl alcohol-alginate encapsulated beads for cadmium ions removal. *Korean J. Chem. Eng.* **2015**, *32*, 1094–1100. [[CrossRef](#)]
40. Jo, W.K.; Clament Sagaya Selvam, N. Enhanced visible light-driven photocatalytic performance of ZnO-g-C₃N₄ coupled with graphene oxide as a novel ternary nanocomposite. *J. Hazard. Mater.* **2015**, *299*, 462–470. [[CrossRef](#)] [[PubMed](#)]
41. Gu, N.; Gao, J.; Wang, K.; Yang, X.; Dong, W. ZnO–montmorillonite as photocatalyst and flocculant for inhibition of cyanobacterial bloom. *Water Air Soil Pollut.* **2015**, *226*, 136. [[CrossRef](#)]
42. Kolodziejczak-Radzimska, A.; Jesionowski, T. Zinc oxide—from synthesis to application: A review. *Materials* **2014**, *7*, 2833–2881. [[CrossRef](#)] [[PubMed](#)]
43. Feng, X.; Guo, H.; Patel, K.; Zhou, H.; Lou, X. High performance, recoverable Fe₃O₄/ZnO nanoparticles for enhanced photocatalytic degradation of phenol. *Chem. Eng. J.* **2014**, *244*, 327–334. [[CrossRef](#)]
44. Ökte, A.N.; Karamanis, D. A novel photoresponsive ZnO-flyash nanocomposite for environmental and energy applications. *Appl. Catal. B Environ.* **2013**, *142–143*, 538–552. [[CrossRef](#)]
45. Ahmad, M.; Ahmed, E.; Hong, Z.L.; Xu, J.F.; Khalid, N.R.; Elhissi, A.; Ahmed, W. A facile one-step approach to synthesizing ZnO/graphene composites for enhanced degradation of methylene blue under visible light. *Appl. Surf. Sci.* **2013**, *274*, 273–281. [[CrossRef](#)]
46. Bailey, S.W.; Brindley, G.W.; Kodama, H.; Martin, R.T. Report of the clay-minerals-society nomenclature committee for 1980–1981—Nomenclature for regular interstratifications. *Clays Clay Miner.* **1982**, *30*, 76–78. [[CrossRef](#)]
47. Guo, Y.; Zhang, G.; Gan, H. Synthesis, characterization and visible light photocatalytic properties of Bi₂WO₆/rectorite composites. *J. Colloid Interface Sci.* **2012**, *369*, 323–329. [[CrossRef](#)] [[PubMed](#)]
48. Lu, Y.; Chang, P.R.; Zheng, P.; Ma, X. Rectorite–TiO₂–Fe₃O₄ composites: Assembly, characterization, adsorption and photodegradation. *Chem. Eng. J.* **2014**, *255*, 49–54. [[CrossRef](#)]
49. Li, S.Q.; Zhou, P.J.; Zhang, W.S.; Chen, S.; Peng, H. Effective photocatalytic decolorization of methylene blue utilizing ZnO/rectorite nanocomposite under simulated solar irradiation. *J. Alloys Compd.* **2014**, *616*, 227–234. [[CrossRef](#)]
50. Wu, S.; Fang, J.; Xu, W.; Cen, C. Bismuth-modified rectorite with high visible light photocatalytic activity. *J. Mol. Catal. A Chem.* **2013**, *373*, 114–120. [[CrossRef](#)]
51. Zhang, Y.; Guo, Y.; Zhang, G.; Gao, Y. Stable TiO₂/rectorite: Preparation, characterization and photocatalytic activity. *Appl. Clay Sci.* **2011**, *51*, 335–340. [[CrossRef](#)]

52. Bu, X.Z.; Zhang, G.K.; Gao, Y.Y.; Yang, Y.Q. Preparation and photocatalytic properties of visible light responsive n-doped TiO₂/rectorite composites. *Microporous Mesoporous Mater.* **2010**, *136*, 132–137. [[CrossRef](#)]
53. Yang, L.; Liang, G.; Zhang, Z.; He, S.; Wang, J. Sodium alginate/Na⁺-rectorite composite films: Preparation, characterization, and properties. *J. Appl. Polym. Sci.* **2009**, *114*, 1235–1240. [[CrossRef](#)]
54. Xiong, G.; Pal, U.; Serrano, J.G.; Ucer, K.B.; Williams, R.T. Photoluminescence and ftir study of ZnO nanoparticles: The impurity and defect perspective. *Phys. Status Solid* **2006**, *3*, 3577–3581. [[CrossRef](#)]
55. Wang, X.; Liu, B.; Ren, J.; Liu, C.; Wang, X.; Wu, J.; Sun, R. Preparation and characterization of new quaternized carboxymethyl chitosan/rectorite nanocomposite. *Compos. Sci. Technol.* **2010**, *70*, 1161–1167. [[CrossRef](#)]
56. Li, Z.; Jiang, W.T.; Hong, H. An ftir investigation of hexadecyltrimethylammonium intercalation into rectorite. *Spectrochim. Acta Part A* **2008**, *71*, 1525–1534. [[CrossRef](#)] [[PubMed](#)]
57. Nguyen, H.D.; Nguyen, T.D.; Nguyen, D.H.; Nguyen, P.T. Magnetic properties of Cr doped Fe₃O₄ porous nanoparticles prepared through a co-precipitation method using surfactant. *Adv. Nat. Sci. Nanosci. Nanotechnol.* **2014**, *5*, 035017. [[CrossRef](#)]
58. Oliveira, L.C.A.; Gonçalves, M.; Guerreiro, M.C.; Ramalho, T.C.; Fabris, J.D.; Pereira, M.C.; Sapag, K. A new catalyst material based on niobia/iron oxide composite on the oxidation of organic contaminants in water via heterogeneous fenton mechanisms. *Appl. Catal. A Gen.* **2007**, *316*, 117–124. [[CrossRef](#)]
59. Shirafuji, T.; Nomura, A.; Hayashi, Y.; Tanaka, K.; Goto, M. Matrix-assisted laser desorption ionization time-of-flight mass spectrometric analysis of degradation products after treatment of methylene blue aqueous solution with three-dimensionally integrated microsolution plasma. *Jpn. J. Appl. Phys.* **2016**, *55*. [[CrossRef](#)]
60. Yang, K.; Zhu, L.; Xing, B. Adsorption of polycyclic aromatic hydrocarbons by carbon nanomaterials. *Environ. Sci. Technol.* **2006**, *40*, 1855–1861. [[CrossRef](#)] [[PubMed](#)]



© 2018 by the authors. Licensee MDPI, Basel, Switzerland. This article is an open access article distributed under the terms and conditions of the Creative Commons Attribution (CC BY) license (<http://creativecommons.org/licenses/by/4.0/>).